

# Improved entanglement entropy estimates from filtered bitstring probabilities

Avi Kaufman, James Corona, Zane Ozzello, Muhammad Asaduzzaman, and Yannick Meurice  
*Department of Physics and Astronomy, The University of Iowa, Iowa City, IA 52242, USA*

(Dated: November 12, 2024)

The von Neumann entanglement entropy provides important information regarding critical points and continuum limits for analog simulators such as arrays of Rydberg atoms. The easily accessible mutual information associated with the bitstring probabilities of complementary subsets  $A$  and  $B$  of one-dimensional quantum chains, provide reasonably sharp lower bounds on the corresponding bipartite von Neumann quantum entanglement entropy  $S_A^{vN}$ . Here, we show that these bounds can in most cases be improved by removing the bitstrings with a probability lower than some value  $p_{min}$  and renormalizing the remaining probabilities (filtering). Surprisingly, in some cases, as we increase  $p_{min}$  the filtered mutual information tends to plateaus at values very close to  $S_A^{vN}$  over some range of  $p_{min}$ . We discuss the dependence on the size of the system, the lattice spacing, and the bipartition of the system. These observations were found for ladders of Rydberg atoms using numerical methods. We also compare with analog simulations involving Rubidium atoms performed remotely with the Aquila device.

**Introduction.** Recent progress in the controlled manipulation of small quantum systems has opened the possibility of using quantum devices to study aspects of lattice models considered in condensed matter or high energy physics which cannot be obtained efficiently with classical computing [1, 2]. In this context, arrays of Rydberg atoms have been used to build quantum simulators for lattice gauge theory models [3–12]. A specific example of quantum simulator is a ladder of Rydberg atoms. Initially designed to simulate scalar QED [7], it does not provide an exact match to the target model [13]. However it has a very rich phase diagram that includes Berezinskii–Kosterlitz–Thouless transition, Conformal Field Theory critical points and incommensurate (floating) phases [14]. This offers multiple opportunities to define continuum limits in regions of parameter space where the correlation lengths are large compared to the lattice spacing. Exploring large parameter spaces to identify the critical regions requires efficient methods.

An important quantity to study phase transitions and the critical behavior is the entanglement entropy [15–31]. The experimental measurement of entanglement entropy is challenging due to its nonlocal nature. One possibility is to prepare and interfere copies of the original system [29–36]. This is experimentally feasible, however it remains labor consuming and not the ideal tool for extensive phase space exploration. Recently it was empirically observed [37] that for arrays of Rydberg atoms, the classical mutual information  $I_{AB}^X$  for a bipartition  $AB$  obtained from the easily accessible bitstring distributions of a single copy, provides a reasonably tight lower bound for the quantum von Neumann entropy  $S_A^{vN} = S_B^{vN}$ . The lower bound property

$$I_{AB}^X \leq S_B^{vN} = S_A^{vN}, \quad (1)$$

follows from Holevo bound [37–39].

In this work we show that this bound can be improved by “filtering” or “truncating” the bitstring probabilities, which means removing the measurements which occur less than a given number of times and renormalizing the

kept measurements. This can be achieved by ignoring measurements of states  $|\{n\}\rangle$  such that the fraction of observations  $N_{\{n\}}/N_{shots} \leq p_{min}$ . In the supplementary material of [37], it was observed that when the ramping down of the Rabi frequency before measurement was too slow, large probabilities were amplified and small probabilities reduced. This has resemblance to the filtering described above. It was then shown that for samples of 1000 bitstrings, removing the states with less than 10 observations ( $p_{min} = 0.01$ ), increased  $I_{AB}^X$  in 6 out of 7 examples considered. In the following, we discuss systematically the effect of  $p_{min}$  on the mutual information  $I_{AB}^X(p_{min})$ . To our surprise, it was found that in some cases, the increase in mutual information was followed by plateaus where  $I_{AB}^X(p_{min}) \simeq S_A^{vN}$ . A particularly convincing illustration is shown in Fig. 1. The dashed line represents an accurate value of  $I_{AB}^X$  without filtering. Almost no changes occur for  $p_{min} \leq 10^{-4}$ , then, as we increase  $p_{min}$  up to  $10^{-2}$ ,  $I_{AB}^X(p_{min})$  transitions from the unfiltered value to values close to  $S_A^{vN}$ .

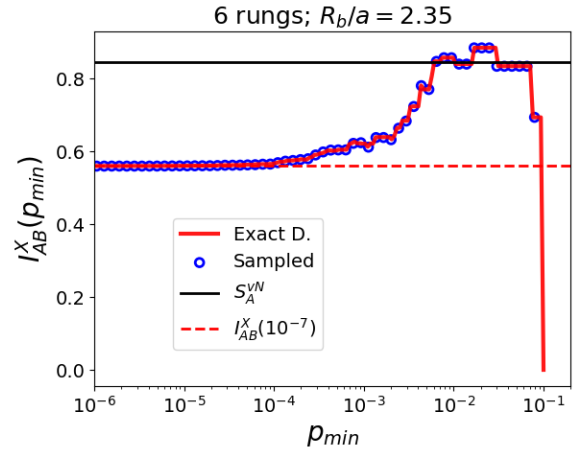


FIG. 1:  $I_{AB}^X(p_{min})$  for a six-rung ladder with exact diagonalization (continuous line) and DMRG sampling (open circles). Details are provided in the text.

In the following, we introduce the specific model used for calculations, a ladder of Rydberg atoms, and perform calculations with exact diagonalization, DMRG methods and, remote operation of the Aquila facilities. We discuss the dependence of the truncated mutual information on the size of the system, the lattice spacing, and the bipartition of the system. This provides a more nuanced picture than the specific example of Fig. 1. Our conclusions involve a discussion of the consequences for experiments with significantly limited amounts of shots.

**The simulator: ladder of Rydberg atoms.** Recently, it has become possible to create arrays of Rydberg atoms with adjustable geometries [40–45]. Their Hamiltonian reads

$$H = \frac{\Omega}{2} \sum_i (|g_i\rangle \langle r_i| + |r_i\rangle \langle g_i|) - \Delta \sum_i n_i + \sum_{i < j} V_{ij} n_i n_j, \quad (2)$$

with van der Waals interactions  $V_{ij} = \Omega R_b^6 / r_{ij}^6$ , for a distance  $r_{ij}$  between the atoms labelled as  $i$  and  $j$ . We use  $\hbar = 1$  units. By definition,  $r_{ij} = R_b$ , the Rydberg blockade radius, when  $V_{ij} = \Omega$  the Rabi frequency. We define the Rydberg occupation  $n_i |r_i\rangle = |r_j\rangle$  while  $n_i |g_i\rangle = 0$ . In the following, we focus on a two leg ladder where the rung length  $a_y$  is twice the distance between rungs  $a_x$ , which is also the lattice spacing denoted  $a$  hereafter. This is illustrated in Fig. 2. This choice is motivated by the rich critical behavior observed in Ref. [14] especially for  $R_b/a \simeq 2.35$  for sufficiently large volume. However, we used open boundary condition for a rectangular shape rather than shifted boundary conditions in [14]. We conducted numerical calculations using density matrix renormalization group (DMRG) [46] and remote analog quantum simulations using the QuEra’s Aquila device [47] which is publicly available. Details are provided in the Appendix.

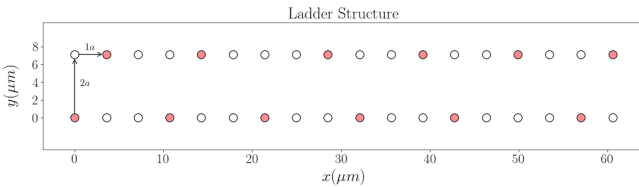


FIG. 2: Illustration of the lattice structure for an 18 rung ladder with ground state (empty circle) and Rydberg state (red circle) atoms.

**Bipartite setup.** For a Rydberg array with  $N_q$  atoms either in the ground  $|g\rangle$  or Rydberg  $|r\rangle$  the whole system ( $AB$ ) can be divided in two subsystems  $A$  and  $B$ . The computational basis consists of the  $2^{N_q}$  elements

$$|\{n\}\rangle \equiv |n_0, n_1, \dots, n_{N_q-1}\rangle, \quad (3)$$

with  $n_j = 0$  or 1 representing  $|g\rangle$  and  $|r\rangle$  respectively. Note that some authors use the opposite convention. Any element of this basis can be factored in a bi-partite way

by splitting the  $N_q$  qubits into  $N_{qA}$  and  $N_{qB}$  qubits with  $N_q = N_{qA} + N_{qB}$ .

$$|\{n\}_{AB}\rangle = |\{n\}_A\rangle |\{n\}_B\rangle, \quad (4)$$

with

$$|\{n\}_A\rangle \equiv |n_0, n_1, \dots, n_{N_{qA}-1}\rangle \text{ and} \quad (5)$$

$$|\{n\}_B\rangle \equiv |n_{N_{qA}}, \dots, n_{N_{qA}+N_{qB}-1}\rangle \quad (6)$$

Given an arbitrary prepared state  $|\psi\rangle$ , we can expand it in the computational basis

$$|\psi\rangle = \sum_{\{n\}} c_{\{n\}} |\{n\}\rangle, \quad (7)$$

The reduced density matrix is defined as  $\rho_A = \text{Tr}_B(\rho_{AB})$ . The von Neumann entanglement entropy is

$$S_A^{vN} = -\text{Tr}_A(\rho_A \ln(\rho_A)) = -\sum_m \lambda_m \ln(\lambda_m), \quad (8)$$

with  $\lambda_m$  the eigenvalues of  $\rho_A$  which are independent of the basis used in  $A$ . The state  $|\{n\}\rangle$  will be observed with a probability

$$p_{\{n\}} = |c_{\{n\}}|^2. \quad (9)$$

These probabilities can be estimated by measurements and we define their experimental Shannon entropy as

$$S_{AB}^X \equiv -\sum_{\{n\}} p_{\{n\}} \ln(p_{\{n\}}), \quad (10)$$

associated with the state  $|\psi\rangle$ . Following Shannon [48] we also define the reduced probability in the subsystem  $A$  by summing over  $B$ :

$$p_{\{n\}_A} = \sum_{\{n\}_B} p_{\{n\}_A \{n\}_B}, \quad (11)$$

and the corresponding reduced entropy

$$S_A^X \equiv -\sum_{\{n\}_A} p_{\{n\}_A} \ln(p_{\{n\}_A}). \quad (12)$$

Similarly, we can define  $S_B^X$  by interchanging  $A$  and  $B$  in the above equations. The classical mutual information is defined as

$$I_{AB}^X \equiv S_A^X + S_B^X - S_{AB}^X. \quad (13)$$

It was already found by Shannon [48] that this quantity is always positive or zero. Upper bounds can also be found by reducing  $\rho_A$  to the diagonal part  $\rho_A^X$  [49, 50]. In summary [37–39] we have the bounds:

$$0 \leq I_{AB}^X \leq S_B^{vN} = S_A^{vN} \leq S_A^X (\text{or } S_B^X). \quad (14)$$

Illustrations of the behavior of these quantities as functions of the adjustable parameters are given in Appendix A in the case of a six-rung ladder.

**Detailed features of Fig.1.** As mentioned in the introduction, Fig. 1 has features that appear in other models and we first discussed them in general. We now discuss more specific aspects. We calculated the vacuum of a 6 rung ladder with  $R_b/a=2.35$ . This first choice of lattice spacing was motivated by the rich critical behavior found in Ref. [14]. We first used exact diagonalization and extracted an accurate value for  $S_A^{vN} \simeq 0.844$  (top horizontal line in Fig.1) for  $A$  being the 3 rungs on say the left side of the ladder. We then calculated the probabilities to observe any of the 4096 states available in the computational basis and obtained the mutual information  $I_{AB}^X \simeq 0.559$  which is about 30 percent below  $S_A^{vN}$  (dashed line). We then removed the states with a probability less than  $p_{min}$ , starting with  $p_{min} = 10^{-6}$ , renormalized the remaining probabilities and then recalculated the filtered  $I_{AB}^X(p_{min})$ .

We then repeated the vacuum calculation using MPS and the DMRG method to generate  $10^7$  random states with probabilities corresponding to the  $|c_n|^2$  using a recursive method available with ITensor (see Appendix B). This can be thought to be an ideal experiment with  $10^7$  shots. The results are in excellent agreement with the exact diagonalization which validates the DMRG method that will be used for larger volumes when exact diagonalization becomes difficult.

**Effects of the filtration on  $S_A^{vN}$ .** It should be noted that in Fig.1, the truncated mutual information gets slightly larger than  $S_A^{vN}$  which seems to conflict with the bound in Eq. (14). For instance,  $I_{AB}^X(0.01) \simeq 0.857 > S_A^{vN} \simeq 0.844$ . However, it should be remembered that the truncated probability distribution is the diagonal part of the truncated density matrix. Calculating  $S_A^{vN}$  for the density matrix obtained with the truncated ground state (see below), we obtain  $S_A^{vN}(0.01) \simeq 1.132$  which is consistent with the bound.

In general we can introduce a projector corresponding to a given filtration

$$P(p_{min}) = \sum_{\{n\}: P_{\{n\}} \geq p_{min}} |\{n\}\rangle \langle \{n\}|. \quad (15)$$

Given a state  $|\psi\rangle$ , we define the normalized projected state as

$$|\psi, p_{min}\rangle = P(p_{min}) |\psi\rangle / \sqrt{\langle \psi | P(p_{min}) | \psi \rangle} \quad (16)$$

and the corresponding density matrix and entropies. We then have the bound

$$I_{AB}^X(p_{min}) \leq S_B^{vN}(p_{min}) = S_A^{vN}(p_{min}). \quad (17)$$

As shown in Fig. 3 this bound is well obeyed in general. Moreover, the distance between the bound and the target value stays more or less constant ( $\simeq 0.3$ ).

**Where should we stop?** Since the filtered mutual information is not necessarily a lower bound of the unfiltered  $S_A^{vN}$ , we need to determine the optimal value of  $p_{min}$ . Fig. 1 suggests that we could stop when  $I_{AB}^X$  stops

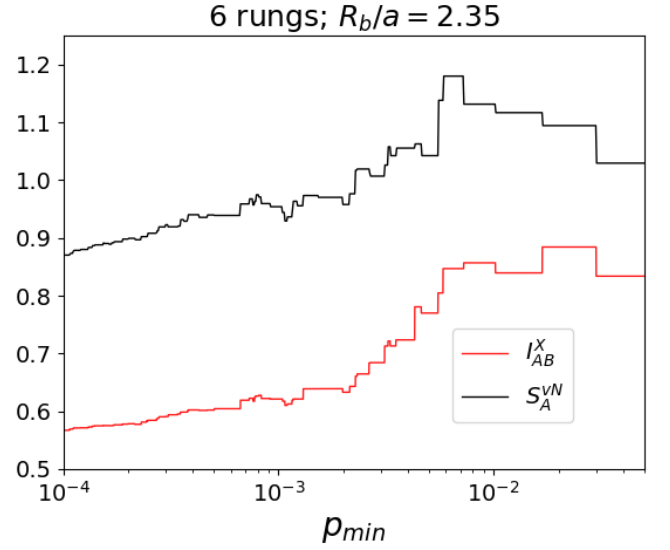


FIG. 3:  $I_{AB}^X(p_{min})$  and  $S_A^{vN}(p_{min})$  for a six-rung ladder with exact diagonalization.

increasing over a “significant” range. Note that there are short range fluctuations due to the discrete nature of the probabilities which are clearly seen on Fig. 3. Consequently the non-increasing property should be seen for scales larger than the fluctuations.

**Volume dependence.** We repeated the procedure described for Fig. 1 but with more rungs. The results are shown in Fig. 4. We see that up to 18 rungs, if we terminate the truncation process when the mutual information stops growing we obtain better estimates of  $S_A^{vN}$  than the untruncated ones. For 20 rungs,  $I_{AB}^X(p_{min})$  decreases over a large part of the left side and this suggests to pick the untruncated value which is actually a rather tight lower bound. For 22 rungs, the first obvious peak overshoots the exact  $S_A^{vN}$  by an amount comparable to the error for the untruncated lower bound. There are some short plateaus which may be considered as more conservative choices.

**Lattice spacing dependence.** We have considered the effect of changing the lattice spacing on  $I_{AB}^X(p_{min})$ . For  $R_b/a = 1.00$ , the entanglement is very low and so is  $I_{AB}^X(p_{min})$  over a broad range on the left. For  $R_b/a$  between 1.25 and 2.25, there are some significant plateaus at values between the untruncated  $I_{AB}^X$  and  $S_A^{vN}$ . For  $R_b/a$  between 2.5 and 3.00, there are in addition broader plateaus at values very slightly above  $S_A^{vN}$ . Again some judgement is required.

**Bipartition dependence.** This method of estimating entanglement entropy is not limited to just even bipartitions of a system. This is shown in Fig. 6 where a Rydberg ladder of 8 rungs and  $R_b/a = 2.35$  is investigated. The methodology is just the same as before, using Eq. (13), but now the sizes  $|A|$  and  $|B|$  need not be equal. In the figure, subsystems go 1 and 7, 2 and 6, etc. The

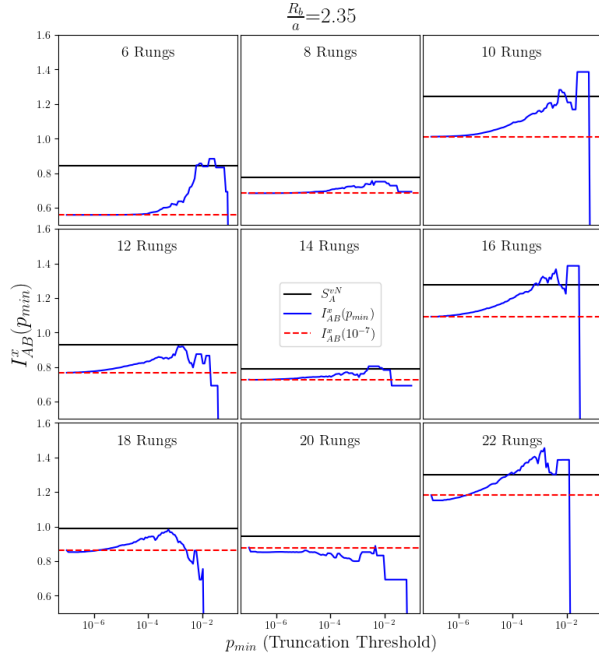


FIG. 4: Effects of the system size on  $I_{AB}^X(p_{min})$  for 6, 8, ..., 22 rungs,  $R_b/a = 2.35$  and 10 million counts obtained via DMRG.

graphs will mirror for the opposite pairings, e.g. subsystems of 1 and 7 have an equivalent graph to 7 and 1. When incorporating the filtered probabilities with varying subsystems it is observed that the filtration reaches closer to the von Neumann entropy when the von Neumann entropy is lower. In Fig. 7, this behavior is shown. A value  $p_{min} = 10^{-2}$  is chosen as it is the approximate best improvement for all subsystem sizes in Fig. 6. To find this  $p_{min}$  exactly in a routine way will be a goal of future work.

**Analog simulations with Aquila.** So far we relied on numerical methods to obtain vacuum states and their associated probabilities. In this subsection, we discuss results obtained by adiabatically preparing the vacuum states and then performing measurements using Quera's Aquila Rydberg atom device. See Appendix D for more information. We performed computations for three different sizes and at three different  $R_b/a$  at fixed  $\Delta/\Omega = 3.5$ . The results are shown in Fig. 8. We observe that some of the qualitative features of the filtered classical mutual information are consistent with the DMRG computation. In some cases, we observe an increase in the filtered mutual information as we increase  $p_{min}$ . However, the position of the peak in the filtered entropy doesn't always coincide with the DMRG computation. All the Aquila quantum simulations approximately use the same number of shots ( $\sim 2000$ ) and we find better agreement for the smaller ladder. Since the process involves characterizing all states including low probability states, and the Hilbert space grows exponentially with

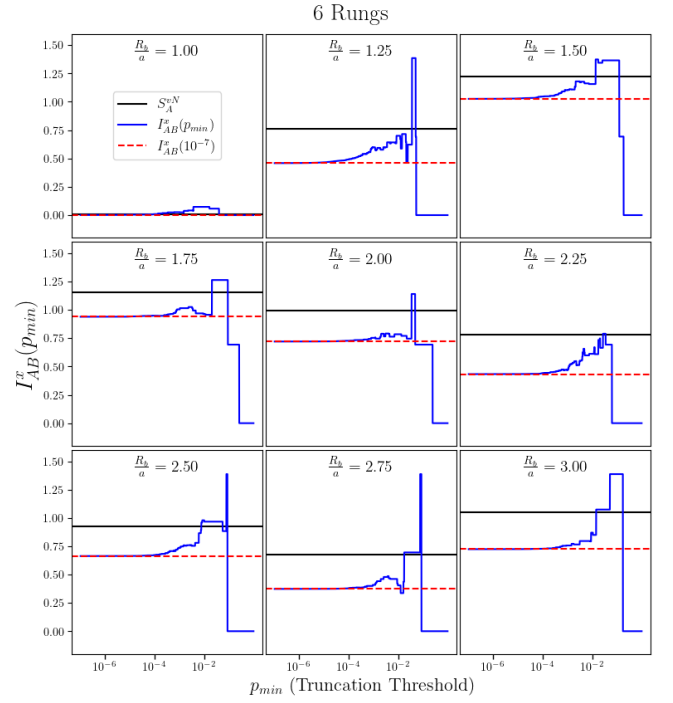


FIG. 5: Effects of the lattice spacing on  $I_{AB}^X(p_{min})$  for  $R_b/a = 1.0, 1.25, \dots, 3.0$ , 6 rungs and 10 million counts obtained via DMRG.

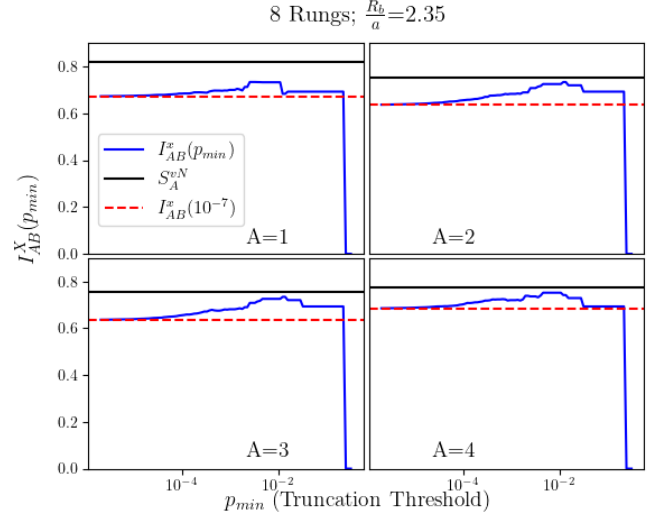


FIG. 6: Illustration of the effects of truncation for differing subsystem sizes for a bipartition. This behavior mirrors for equivalent sizing. Probabilities obtained with 10 million counts of DMRG.

the number of atoms ( $\dim(H) \propto 2_q^N$ ), recovering quantitative result for the filtered mutual information can become problematic with a low number of shots due to large statistical errors on low probability measurements.

Using DMRG results, Appendix C shows that significant deviations are expected when the simulation is run

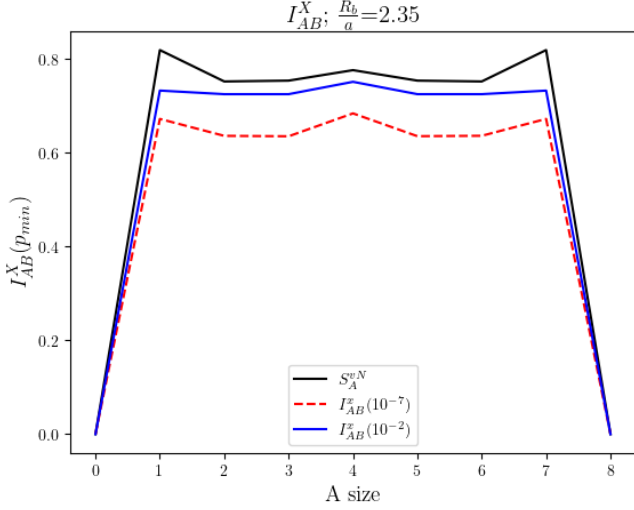


FIG. 7: Illustration of the effects of bipartition across the von Neumann entropy, mutual information, and truncation of mutual information. Probabilities obtained with 10 million counts of DMRG.

with thousand measurements. Appendix E shows that for Aquila data, the source of error is not just statistical in nature. A more systematic analysis of the discrepancies and possible mitigation are under investigation.

**Conclusions.** Using examples of ladders of Rydberg atoms, we have shown that by excluding bitstrings with probabilities lower than  $p_{min}$  and renormalizing the remaining data, a procedure that we call filtering, we tend to obtain larger mutual information and better approximations to the von Neumann entanglement entropy  $S_A^{vN}$ . As the filtered mutual information does not in general provide a lower bound on  $S_A^{vN}$ , the optimal value for  $p_{min}$  requires some discussion. A conservative approach would be to stop when the mutual information stops increasing over a range of  $p_{min}$  which is large compared to the range for small fluctuations due to the discrete nature of the probabilities. In a significant number of cases considered, we found consistent plateaus where the filtered mutual information closely approximates  $S_A^{vN}$  over a broad range of values. The reasons for this behavior is currently under investigation.

Analog simulations with a few thousands shots provide a limited access to states with low probabilities and naturally provide significantly filtered data. The origin of the discrepancies between Aquila data and numerical methods is currently under investigation. Future work may extend these techniques to larger systems and more complex geometries, furthering their applications for analog simulations.

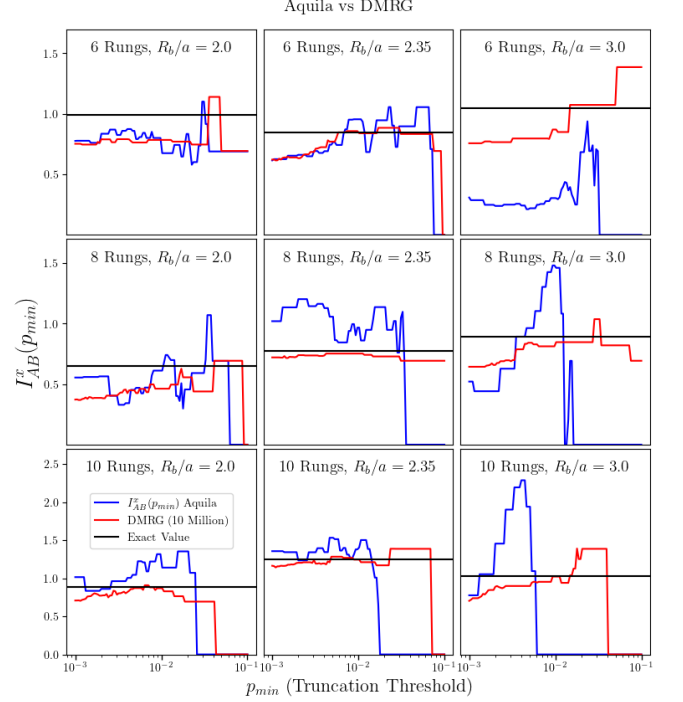


FIG. 8: Filtered mutual information obtained from DMRG (10 million counts) vs Aquila (1000 shots) for various  $R_b/a$  (2.0, 2.35 and 3.0) and system sizes (6, 8 and 10 rungs).

## Acknowledgements

This research was supported in part by the Dept. of Energy under Award Number DE-SC0019139. We thank the Amazon Web Services and S. Hassinger for facilitating remote access to QuEra through the Amazon Braket while teaching quantum mechanics and our Department of Physics and Astronomy for supporting part of the cost of the analog simulations presented here. We thank the University of Iowa for providing access to the Argon computing facilities. We acknowledge the use of NERSC facilities with ERCAP 0023235 award.

## Appendix A: Phase diagram and bound on entanglement entropy

In this appendix, we present the entanglement entropy for a six-rung ladder as a function of  $R_b/a$  and  $\Delta/\Omega$ . The results are shown in Fig. 9. For small systems, the results are sensitive to the system size and boundary conditions. For a detailed overview on different phases in the Rydberg ladder at larger volumes and different boundary conditions see [14].

In Fig. 10, we plotted the bitstring entropy  $S_{AB}^X$ , the reduced bitstring entropy  $S_A^X$ , the von Neumann entropy  $S_A^{vN}$  and the classical mutual information  $I_{AB}^X$  as we vary the inverse lattice spacing in blockade-radius unit. We observe agreement with the rigorous bounds  $0 \leq I_{AB}^X \leq$



$S_A^{vN} \leq S_A^X$ . We also observe that  $S_A^{vN}$  becomes larger when the gap closes.

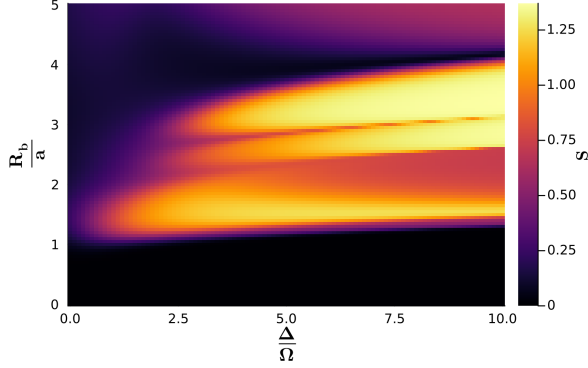


FIG. 9: von Neumann entanglement entropy for a six-rung ladder with  $a_y = 2a_x$  as a function of  $R_b/a_x$  and  $\Delta/\Omega$ .

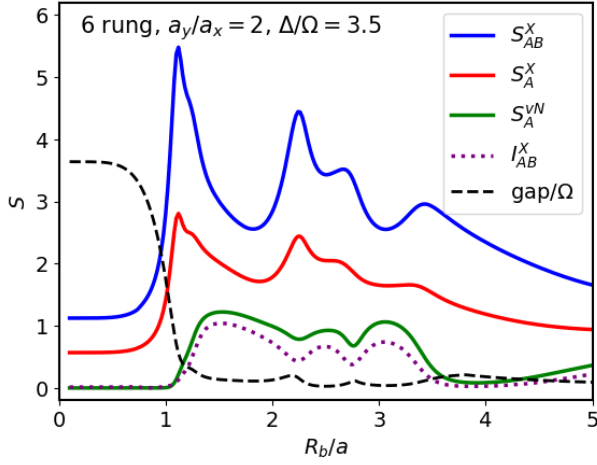


FIG. 10: Comparison of  $S_{AB}^X$ ,  $S_A^X$ ,  $S_A^{vN}$  and  $I_{AB}^X$  at a fixed  $\Delta/\Omega = 3.5$ .

## Appendix B: Numerical methods

Numerical calculations were performed with  $\Omega = 5\pi$  MHz, which implies  $R_b = 8.375\mu\text{m}$ , and a detuning  $\Delta = 17.5\pi$  MHz as in [14].  $R_b/a$  was varied between 1 and 3. Exact diagonalization calculations were performed in python using the linalg library. The DMRG calculations of vacua and the samples of measurements with the corresponding probability were performed with the ITensor software library in Julia [51].

## Appendix C: Fluctuations in finite sampling

With the current technology, the number of shots obtained in analog simulations is much lower than the 10 million shots obtained with the DMRG. Using QuEra's Aquila device [47] we are able to produce 1000 shots on a consistent basis. In order to produce DMRG data that resembles experimental output, we randomly reduce our sample size to 1000 shots. To see the impact a smaller sample size has on the error of the mutual information, we do this smaller sample size 1000 times. From these 1000 samples of 1000 shots we calculate error bars. Fig. 11 shows the high accuracy DMRG (10 million shots) plotted against the Sampled DMRG (1000 shots) with errors bars. The figure shows that the randomly selected DMRG subsamples roughly follow the shape of the higher accuracy DMRG. This puts the analog calculation discrepancies in perspective.

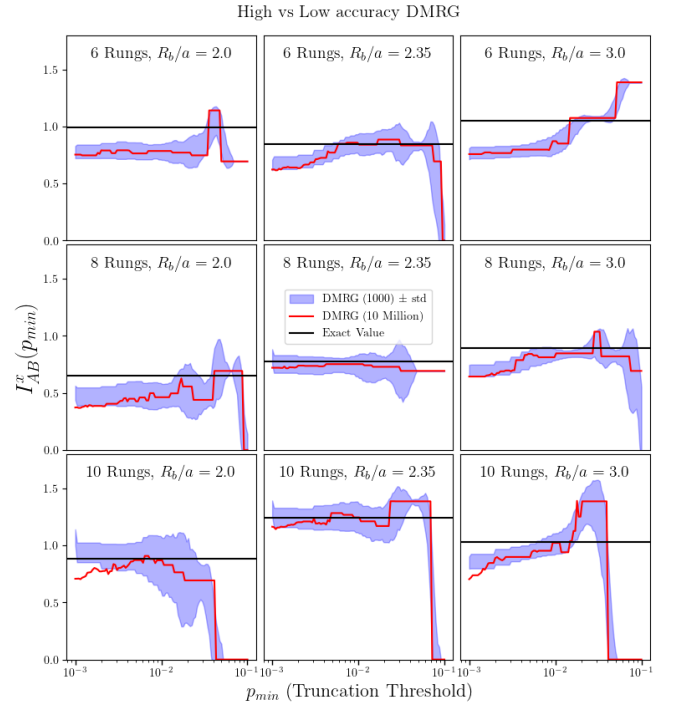


FIG. 11: DMRG (10 million counts) vs DMRG (1000 shots with error) for various  $R_b/a$  and system sizes.

## Appendix D: Quantum device simulation methods

We conducted remote analog quantum simulations using QuEra's Aquila device [47]. The motivation behind this is to investigate larger system sizes which at some point will become inaccessible with classical computation methods. With the naive exact diagonalization we could investigate a Rydberg system of size  $N_q = 12$ , whereas

with high-precision DMRG calculation we could investigate up to a system size  $N_q = 44$ . In the near future, we will be able to investigate models with far more atoms than this with the quantum device. Aquila has a roadmap for extending their device to simulate more than 3000 atoms by 2025 [52]. However, since the jobs at hand amounts to performing tomography, the resource requirement of gathering useful statistics increases exponentially in the number of shots. We presented filtering mutual information calculated from the Aquila device for a maximum system size of  $L = 10$  rungs. We are currently investigating what causes the results to deviate, and the work will be reported elsewhere.

We prepared the ground state of the system adiabatically. Initially we prepare a state with all the atoms in the ground state. Incidentally, this is the ground state of the Rydberg system at infinite negative detuning and zero Rabi frequency. Next, we slowly tune the Rabi frequency from zero to the target frequency ( $\Omega$ ) and in the same duration, we increase the detuning from a large negative value to the target value ( $\Delta$ ). Ideally due to the slow adiabatic evolution we can reach the ground state of the target parameters as the system is gapped. In experiments, before any measurement is performed, Rabi frequency is switched off as this is essential for the fluorescence imaging in the readout process [40]. This is done as fast as possible so that the ground state of the target Hamiltonian is minimally disrupted by other low lying energy states. There are different choices on how to tune the parameters in the Rydberg simulation to prepare ground state at different phases. Once we set the lattice spacing  $a$  to a fixed number, we can set the final Rabi frequency and final detuning to different values to recover the ground state at different phases. For the Aquila simulation, we use the same parameters to that of DMRG simulation in all the cases, except for the case  $R_b/a = 3.0$ , where we use  $\Omega = 0.4982\pi$  MHz due to the geometrical constraint that distance between two nearest neighbor atoms needs to be less than  $4 \mu\text{m}$  at the current publicly available setup at Aquila device.

### Appendix E: Sources of error in the analog simulations

We performed a comparison of the variation in shot counts for the computation of filtered mutual information. It is clear from Fig. 12 that for  $L = 6$ , increasing the number of shots reduces the error in the filtered data obtained from the quantum device. However, there are other sources of error that are not mitigated – even for small ladder with  $L = 6$  rungs. The sources of these errors in such simulations and potential mitigation strategies are currently under investigation, and the results will be presented in a future work.

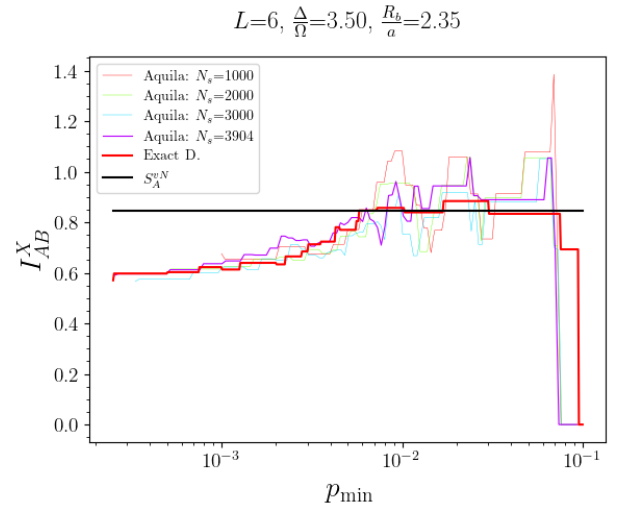


FIG. 12: The number of shots is varied to investigate the deviation of the Aquila simulation result with the exact diagonalization.

- 
- [1] Christian W. Bauer et al., “Quantum Simulation for High-Energy Physics,” *PRX Quantum* **4**, 027001 (2023), arXiv:2204.03381 [quant-ph].
- [2] Ehud Altman et al., “Quantum Simulators: Architectures and Opportunities,” *PRX Quantum* **2**, 017003 (2021), arXiv:1912.06938 [quant-ph].
- [3] Jin Zhang, J. Unmuth-Yockey, J. Zeiher, A. Bazavov, S.-W. Tsai, and Y. Meurice, “Quantum simulation of the universal features of the polyakov loop,” *Phys. Rev. Lett.* **121**, 223201 (2018).
- [4] Federica M. Surace, Paolo P. Mazza, Giuliano Giudici, Alessio Lerose, Andrea Gambassi, and Marcello Dalmonte, “Lattice gauge theories and string dynamics in rydberg atom quantum simulators,” *Phys. Rev. X* **10**, 021041 (2020).
- [5] Simone Notarnicola, Mario Collura, and Simone Montangero, “Real-time-dynamics quantum simulation of  $(1 + 1)$ -dimensional lattice qed with rydberg atoms,” *Phys. Rev. Res.* **2**, 013288 (2020).
- [6] Alessio Celi, Benoît Vermersch, Oscar Viyuela, Hannes Pichler, Mikhail D. Lukin, and Peter Zoller, “Emerging Two-Dimensional Gauge Theories in Rydberg Configurable Arrays,” *Phys. Rev. X* **10**, 021057 (2020), arXiv:1907.03311 [quant-ph].
- [7] Yannick Meurice, “Theoretical methods to design and test quantum simulators for the compact Abelian Higgs model,” *Phys. Rev. D* **104**, 094513 (2021), arXiv:2107.11366 [quant-ph].
- [8] Pierre Fromholz, Mikheil Tsitsishvili, Matteo Votto, Marcello Dalmonte, Alexander Nersisyan, and Titas Chanda, “Phase diagram of rydberg-dressed atoms on two-leg triangular ladders,” *Phys. Rev. B* **106**, 155411 (2022).
- [9] Daniel González-Cuadra, Torsten V. Zache, Jose Carrasco, Barbara Kraus, and Peter Zoller, “Hardware Efficient Quantum Simulation of Non-Abelian Gauge Theories with Qudits on Rydberg Platforms,” *Phys. Rev. Lett.* **129**, 160501 (2022), arXiv:2203.15541 [quant-ph].
- [10] Kenneth Heitritter, Yannick Meurice, and Stephen Mrenna, “Prolegomena to a hybrid Classical/Rydberg simulator for hadronization (QuPYTH),” (2022), arXiv:2212.02476 [quant-ph].
- [11] Jad C. Halimeh, Monika Aidelsburger, Fabian Grusdt, Philipp Hauke, and Bing Yang, “Cold-atom quantum simulators of gauge theories,” (2023), arXiv:2310.12201 [cond-mat.quant-gas].
- [12] Daniel Gonzalez-Cuadra et al., “Observation of string breaking on a  $(2 + 1)$ D Rydberg quantum simulator,” (2024), arXiv:2410.16558 [quant-ph].
- [13] Jin Zhang, Shan-Wen Tsai, and Yannick Meurice, “Critical behavior of lattice gauge theory Rydberg simulators from effective Hamiltonians,” (2023), arXiv:2312.04436 [quant-ph].
- [14] Jin Zhang, Sergio H. Cantú, Fangli Liu, Alexei Bylinskii, Boris Braverman, Florian Huber, Jesse Amato-Grill, Alexander Lukin, Nathan Gemelke, Alexander Keesling, Sheng-Tao Wang, Y. Meurice, and S. W. Tsai, “Probing quantum floating phases in rydberg atom arrays,” (2024), arXiv:2401.08087 [quant-ph].
- [15] Luigi Amico, Rosario Fazio, Andreas Osterloh, and Vlatko Vedral, “Entanglement in many-body systems,” *Reviews of Modern Physics* **80**, 517 (2008).
- [16] J. Eisert, M. Cramer, and M. B. Plenio, “Area laws for the entanglement entropy - a review,” *Rev. Mod. Phys.* **82**, 277–306 (2010), arXiv:0808.3773 [quant-ph].
- [17] Shinsei Ryu and Tadashi Takayanagi, “Holographic derivation of entanglement entropy from AdS/CFT,” *Phys. Rev. Lett.* **96**, 181602 (2006), arXiv:hep-th/0603001.
- [18] Dmitry A. Abanin, Ehud Altman, Immanuel Bloch, and Maksym Serbyn, “Colloquium : Many-body localization, thermalization, and entanglement,” *Reviews of Modern Physics* **91** (2019), 10.1103/revmodphys.91.021001.
- [19] J. Ignacio Cirac, David Perez-Garcia, Norbert Schuch, and Frank Verstraete, “Matrix product states and projected entangled pair states: Concepts, symmetries, theorems,” *Rev. Mod. Phys.* **93**, 045003 (2021), arXiv:2011.12127 [quant-ph].
- [20] Sudip Ghosh, Ronak M Soni, and Sandip P. Trivedi, “On The Entanglement Entropy For Gauge Theories,” *JHEP* **09**, 069 (2015), arXiv:1501.02593 [hep-th].
- [21] Karel Van Acoleyen, Nick Bultinck, Jutho Haegeman, Michael Marien, Volkher B. Scholz, and Frank Verstraete, “The entanglement of distillation for gauge theories,” *Phys. Rev. Lett.* **117**, 131602 (2016), arXiv:1511.04369 [quant-ph].
- [22] Mari Carmen Bañuls, Krzysztof Cichy, J. Ignacio Cirac, Karl Jansen, and Stefan Kühn, “Efficient basis formulation for  $1+1$  dimensional  $SU(2)$  lattice gauge theory: Spectral calculations with matrix product states,” *Phys. Rev. X* **7**, 041046 (2017), arXiv:1707.06434 [hep-lat].
- [23] Johannes Knaute, Matan Feuerstein, and Erez Zohar, “Entanglement and confinement in lattice gauge theory tensor networks,” *JHEP* **02**, 174 (2024), arXiv:2401.01930 [quant-ph].
- [24] Dmitri E. Kharzeev and Eugene M. Levin, “Deep inelastic scattering as a probe of entanglement,” *Phys. Rev. D* **95**, 114008 (2017), arXiv:1702.03489 [hep-ph].
- [25] O. K. Baker and D. E. Kharzeev, “Thermal radiation and entanglement in proton-proton collisions at energies available at the cern large hadron collider,” *Phys. Rev. D* **98**, 054007 (2018).
- [26] Kun Zhang, Kun Hao, Dmitri Kharzeev, and Vladimir Korepin, “Entanglement entropy production in deep inelastic scattering,” *Phys. Rev. D* **105**, 014002 (2022), arXiv:2110.04881 [quant-ph].
- [27] Silas R. Beane, David B. Kaplan, Natalie Klco, and Martin J. Savage, “Entanglement Suppression and Emergent Symmetries of Strong Interactions,” *Phys. Rev. Lett.* **122**, 102001 (2019), arXiv:1812.03138 [nucl-th].
- [28] Caroline Robin, Martin J. Savage, and Nathalie Pillet, “Entanglement Rearrangement in Self-Consistent Nuclear Structure Calculations,” *Phys. Rev. C* **103**, 034325 (2021), arXiv:2007.09157 [nucl-th].
- [29] G. Vidal, J. I. Latorre, E. Rico, and A. Kitaev, “Entanglement in quantum critical phenomena,” *Phys. Rev. Lett.* **90**, 227902 (2003).
- [30] V. E. Korepin, “Universality of entropy scaling in one dimensional gapless models,” *Phys. Rev. Lett.* **92**, 096402 (2004).
- [31] Pasquale Calabrese and John L. Cardy, “Entanglement entropy and quantum field theory: A Non-



- technical introduction,” *Int. J. Quant. Inf.* **4**, 429 (2006), arXiv:quant-ph/0505193.
- [32] Dmitry A. Abanin and Eugene Demler, “Measuring entanglement entropy of a generic many-body system with a quantum switch,” *Phys. Rev. Lett.* **109**, 020504 (2012).
  - [33] A. J. Daley, H. Pichler, J. Schachenmayer, and P. Zoller, “Measuring entanglement growth in quench dynamics of bosons in an optical lattice,” *Phys. Rev. Lett.* **109**, 020505 (2012).
  - [34] Rajibul Islam, Ruichao Ma, Philipp M. Preiss, M. Eric Tai, Alexander Lukin, Matthew Rispoli, and Markus Greiner, “Measuring entanglement entropy in a quantum many-body system,” *Nature* **528**, 77–83 (2015).
  - [35] Adam M. Kaufman, M. Eric Tai, Alexander Lukin, Matthew Rispoli, Robert Schittko, Philipp M. Preiss, and Markus Greiner, “Quantum thermalization through entanglement in an isolated many-body system,” *Science* **353**, 794–800 (2016).
  - [36] J. Unmuth-Yockey, Jin Zhang, P. M. Preiss, Li-Ping Yang, S. W. Tsai, and Y. Meurice, “Probing the conformal Calabrese-Cardy scaling with cold atoms,” *Phys. Rev. A* **96**, 023603 (2017), arXiv:1611.05016 [cond-mat.quant-gas].
  - [37] Yannick Meurice, “Experimental lower bounds on entanglement entropy without twin copy,” (2024), arXiv:2404.09935 [quant-ph].
  - [38] John Preskill and Mehdi Soleimanifar, “Private communication,” (2024).
  - [39] Tai-Hsuan Yang, Mehdi Soleimanifar, Thiago Bergamaschi, and John Preskill, “When can classical neural networks represent quantum states?” (2024), arXiv:2410.23152 [quant-ph].
  - [40] Hannes Bernien, Sylvain Schwartz, Alexander Keesling, Harry Levine, Ahmed Omran, Hannes Pichler, Soonwon Choi, Alexander S. Zibrov, Manuel Endres, Markus Greiner, Vladan Vuletić, and Mikhail D. Lukin, “Probing many-body dynamics on a 51-atom quantum simulator,” *Nature* **551**, 579–584 (2017).
  - [41] Alexander Keesling, Ahmed Omran, Harry Levine, Hannes Bernien, Hannes Pichler, Soonwon Choi, Rhine Samajdar, Sylvain Schwartz, Pietro Silvi, Subir Sachdev, Peter Zoller, Manuel Endres, Markus Greiner, Vladan Vuletić, and Mikhail D. Lukin, “Quantum kibble-zurek mechanism and critical dynamics on a programmable rydberg simulator,” *Nature* **568**, 207–211 (2019).
  - [42] Henning Labuhn, Daniel Barredo, Sylvain Ravets, Sylvain de Léséleuc, Tommaso Macrì, Thierry Lahaye, and Antoine Browaeys, “Tunable two-dimensional arrays of single rydberg atoms for realizing quantum ising models,” *Nature* **534**, 667–670 (2016).
  - [43] Sylvain de Léséleuc, Vincent Lienhard, Pascal Scholl, Daniel Barredo, Sebastian Weber, Nicolai Lang, Hans Peter Büchler, Thierry Lahaye, and Antoine Browaeys, “Observation of a symmetry-protected topological phase of interacting bosons with rydberg atoms,” *Science* **365**, 775–780 (2019).
  - [44] Sepehr Ebadi, Tout T. Wang, Harry Levine, Alexander Keesling, Giulia Semeghini, Ahmed Omran, Dolev Bluvstein, Rhine Samajdar, Hannes Pichler, Wen Wei Ho, Soonwon Choi, Subir Sachdev, Markus Greiner, Vladan Vuletić, and Mikhail D. Lukin, “Quantum phases of matter on a 256-atom programmable quantum simulator,” *Nature* **595**, 227–232 (2021).
  - [45] Pascal Scholl, Michael Schuler, Hannah J. Williams, Alexander A. Eberharter, Daniel Barredo, Kai-Niklas Schymik, Vincent Lienhard, Louis-Paul Henry, Thomas C. Lang, Thierry Lahaye, Andreas M. Läuchli, and Antoine Browaeys, “Quantum simulation of 2d antiferromagnets with hundreds of rydberg atoms,” *Nature* **595**, 233–238 (2021).
  - [46] Ulrich Schollwöck, “The density-matrix renormalization group,” *Reviews of modern physics* **77**, 259–315 (2005).
  - [47] Jonathan Wurtz, Alexei Bylinskii, Boris Braverman, Jesse Amato-Grill, Sergio H. Cantu, Florian Huber, Alexander Lukin, Fangli Liu, Phillip Weinberg, John Long, Sheng-Tao Wang, Nathan Gemelke, and Alexander Keesling, “Aquila: Quera’s 256-qubit neutral-atom quantum computer,” (2023), arXiv:2306.11727 [quant-ph].
  - [48] C.E. Shannon and W. Weaver, *The Mathematical Theory of Communication*, Illini books (University of Illinois Press, 1949).
  - [49] John Preskill, “Quantum information chapter 10. quantum shannon theory,” (2022).
  - [50] Edward Witten, “A Mini-Introduction To Information Theory,” *Riv. Nuovo Cim.* **43**, 187–227 (2020), arXiv:1805.11965 [hep-th].
  - [51] Matthew Fishman, Steven R. White, and E. Miles Stoudenmire, “The ITensor Software Library for Tensor Network Calculations,” *SciPost Phys. Codebases*, 4 (2022).
  - [52] “Quera computing releases a groundbreaking roadmap for advanced error-corrected quantum computers, pioneering the next frontier in quantum innovation,” (2024), accessed: 2024-11-05.